

Radiative effects during the assembly of direct collapse black holes

Aaron Smith,¹* Fernando Becerra,² Volker Bromm¹ and Lars Hernquist²

¹*Department of Astronomy, The University of Texas at Austin, Austin, TX 78712, USA*

²*Department of Astronomy, Harvard University, 60 Garden Street, Cambridge, MA 02138, USA*

Accepted 2017 August 1. Received 2017 July 25; in original form 2017 June 8

ABSTRACT

We perform a post-processing radiative feedback analysis on a 3D ab initio cosmological simulation of an atomic cooling halo under the direct collapse black hole (DCBH) scenario. We maintain the spatial resolution of the simulation by incorporating native ray-tracing on unstructured mesh data, including Monte Carlo Lyman α ($\text{Ly}\alpha$) radiative transfer. DCBHs are born in gas-rich, metal-poor environments with the possibility of Compton-thick conditions, $N_{\text{H}} \gtrsim 10^{24} \text{ cm}^{-2}$. Therefore, the surrounding gas is capable of experiencing the full impact of the bottled-up radiation pressure. In particular, we find that multiple scattering of $\text{Ly}\alpha$ photons provides an important source of mechanical feedback after the gas in the sub-parsec region becomes partially ionized, avoiding the bottleneck of destruction via the two-photon emission mechanism. We provide detailed discussion of the simulation environment, expansion of the ionization front, emission and escape of $\text{Ly}\alpha$ radiation, and Compton scattering. A sink particle prescription allows us to extract approximate limits on the post-formation evolution of the radiative feedback. Fully coupled $\text{Ly}\alpha$ radiation hydrodynamics will be crucial to consider in future DCBH simulations.

Key words: radiative transfer – galaxies: formation – galaxies: high-redshift – cosmology: theory.

1 INTRODUCTION

Quasars powered by black holes with masses up to $\sim 10^{10} M_{\odot}$ have been observed out to a redshift of $z \sim 7$, presenting a timing problem for their growth by conventional accretion (Fan et al. 2006; Mortlock et al. 2011; Wu et al. 2015). In the context of galaxy formation theory, the most plausible explanation for the origin of the first supermassive black holes (SMBHs) is either rapid seeding or unusually efficient growth (Volonteri 2012; Johnson & Haardt 2016; Smith et al. 2017a). In particular, viable candidates include the direct collapse scenario which gives rise to $10^{4-6} M_{\odot}$ seeds under specialized conditions in the early Universe (Bromm & Loeb 2003; Begelman et al. 2006; Lodato & Natarajan 2006; Regan & Haehnelt 2009), and hyper-Eddington accretion on to stellar remnant black holes (Wyithe & Loeb 2012; Pacucci et al. 2015a; Inayoshi et al. 2016). Thereafter, episodic galaxy mergers and cold gas accretion from the cosmic web regulate the growth of nuclear black holes (Li et al. 2007; Mayer et al. 2010; Smidt et al. 2017). The emergence of $M_{\bullet} \lesssim 10^6 M_{\odot}$ black holes within quasar progenitors at $z \gtrsim 10$ is beyond the reach of current telescopes, but should come within reach with the *James Webb Space Telescope* (JWST) (e.g. Natarajan et al. 2017; Dayal et al. 2017). Indeed, different formation scenarios may have unique observational signatures and dynamical implications (Gallerani et al. 2017). Therefore, our understanding of black hole assembly and growth in realistic settings

can have a significant impact on models and simulations of the first galaxies (Bromm & Yoshida 2011). The first SMBHs can affect galaxy evolution through radiative feedback that drives winds, suppresses star formation, and contributes to the reionization of the Universe (Loeb & Furlanetto 2013).

Forming a direct collapse black hole (DCBH) requires primordial gas to collapse without fragmentation. This is achieved by strong non-ionizing Lyman–Werner radiation (LW; $h\nu = 11.2 - 13.6 \text{ eV}$) from neighbouring galaxies which photodissociates H_2 (Agarwal et al. 2012, 2014; Regan et al. 2017). With only atomic hydrogen line cooling available, the gas follows nearly isothermal collapse once the virial temperature reaches $T_{\text{vir}} \sim 10^4 \text{ K}$ (Omukai 2001; Oh & Haiman 2002). DCBHs are thus born in gas-rich environments with no previous star formation. The hydrogen column density when averaged over all directions is extremely high, $N_{\text{H}} \gtrsim 10^{24} \text{ cm}^{-2}$, potentially leading to Compton-thick conditions (Yue et al. 2013). Certainly, the initial assembly environment is self-absorbing to ionizing photons. However, the subsequent evolution remains an open question. In particular, what is the role of radiative feedback? After a certain time-scale metal enrichment from neighbouring galaxies and supernovae from concurrent star formation will alter the surroundings. Eventually, the black hole likely resembles that of typical active galactic nuclei (AGN), undergoing sub-Eddington accretion rates over multiple duty cycles (Milosavljević et al. 2009). However, is the dominant driver of the evolution of DCBHs related to internal or external factors?

A particularly interesting source of feedback in the DCBH

* E-mail: asmith@astro.as.utexas.edu

scenario is Lyman α ($\text{Ly}\alpha$) radiation pressure. As a strong resonant line of neutral hydrogen, $\text{Ly}\alpha$ photons undergo multiple scattering which may enhance the effective $\text{Ly}\alpha$ force by one or two orders of magnitude in optically thick regions (Dijkstra & Loeb 2008, 2009). The first self-consistent $\text{Ly}\alpha$ radiation hydrodynamics (RHD) simulations were performed by Smith et al. (2016, 2017b), who coupled a Monte Carlo radiative transfer (MCRT) code with spherically symmetric Lagrangian frame hydrodynamics including ionizing radiation, non-equilibrium chemistry and cooling, and self-gravity. They found a dense shell-like outflow structure, formed in response to the central ionizing source, and that $\text{Ly}\alpha$ radiation pressure may have a significant dynamical impact on gas surrounding DCBHs. Finally, it has also been suggested that trapped $\text{Ly}\alpha$ cooling radiation may enhance the formation of DCBHs by facilitating the photodetachment of H^- ions, precursors to H_2 , during collapse (Agarwal & Khochfar 2015; Johnson & Dijkstra 2017). However, all $\text{Ly}\alpha$ feedback studies thus far have been limited to 1D geometries.

There is a good reason to believe that SMBH formation scenarios may be observationally testable with the capabilities of next-generation observatories. Indeed, already the luminous COSMOS redshift 7 (CR7) $\text{Ly}\alpha$ emitter at $z = 6.6$ has received substantial attention due to its exceptionally strong $\text{Ly}\alpha$ and possible He II 1640 Å emission with no detection of metal lines from the UV to the near-infrared within instrumental sensitivity (Matthee et al. 2015; Sobral et al. 2015). As a result, CR7 has served as a prominent case study for young primordial starburst and DCBH models (Pallottini et al. 2015; Agarwal et al. 2016; Dijkstra et al. 2016b; Hartwig et al. 2016; Smidt et al. 2016; Smith et al. 2016; Visbal et al. 2016). However, the debate regarding the origin of CR7 remains ongoing, especially after deeper broad-band observations are consistent with a low-mass, narrow-line AGN or stellar models with massive, low-metallicity binaries (Bowler et al. 2017). Furthermore, recent reexamination of the original spectroscopic data lowers the confidence-level of the He II line detection to $< 2\sigma$ (Shibuya et al. 2017). Deeper spectroscopy of CR7 and future candidates will be necessary to convincingly discriminate between a black hole seeded via direct collapse and other more standard interpretations (Agarwal et al. 2017; Pacucci et al. 2017). Still, other observational signatures of DCBHs may be manifest if their spectral energy distributions (SEDs) exhibit the imprint of Compton-thickness (Pacucci et al. 2015b). For example, DCBHs may be responsible for the measured correlations between the cosmic infrared and X-ray backgrounds, i.e. the source-subtracted fluctuations after accounting for foreground stars and galaxies (Kashlinsky et al. 2005; Cappelluti et al. 2013; Helgason et al. 2016). The collection of several independent signatures with next-generation observatories will clarify and constrain our understanding of the first SMBHs.

The primary focus of this paper is to investigate the effects of radiative feedback during DCBH assembly by carrying out a post-processing analysis of the high-resolution ab initio cosmological simulation of Becerra et al. (2017). For this exploratory study, the radiation remains decoupled from the hydrodynamical evolution of the gas. However, we fully explore the impact of $\text{Ly}\alpha$ radiation pressure in a realistic 3D DCBH environment, which is therefore complementary to the work of Smith et al. (2017b). This is important because asymmetries in the gas distribution introduce a directional dependence of the $\text{Ly}\alpha$ spectrum and escape properties (e.g. Behrens et al. 2014; Zheng & Wallace 2014; Smith et al. 2015). Throughout this work, we use the terminology of pre- and post-formation to consider environmental changes due to the buildup

of the massive object (Becerra et al. 2017; Woods et al. 2017). This paper is organized as follows. In Section 2, we discuss details of the simulation setup as well as the physical properties of the host galaxy. In Section 3, we argue that the buildup and eventual breakout of ionizing photons represents a critical transition for the DCBH. In Section 4, we present the $\text{Ly}\alpha$ radiative transfer calculations and discuss the potential impact in relation to other forces acting on the gas. In Section 5, we evaluate the role of Compton scattering in the sub-parsec region around the black hole. Finally, in Section 6, we explore the implications of our work.

2 SIMULATION

2.1 DCBH Formation

We perform a high-resolution ab initio cosmological simulation of the collapse of an atomic cooling halo. Using the approach described in Becerra et al. (2015) and Becerra et al. (2017), we follow the evolution of the halo from cosmological initial conditions at redshift $z = 99$ until its collapse at $z \approx 11.6$. Fig. 1 shows the projected gas density of the central 25 kpc, 1.25 kpc, 50 pc and 2.5 pc from left to right, which illustrates the morphology of the halo from the large-scale environment down to the central gas cloud. We emulate the formation of a DCBH by inserting a sink particle once the highest density cell reaches a threshold number density of $n_{\text{th}} \approx 10^8 \text{ cm}^{-3}$. The accretion radius of this particle is set to $R_{\text{acc}} = 1 \text{ pc}$ (Becerra et al. 2017) in such a way that the initial mass of the sink particle is $M_{\bullet} \approx 8.8 \times 10^4 M_{\odot}$. Thus, the post-formation scenario should be interpreted as an aggressive extrapolation of the DCBH environment without fully resolving the formation and growth of the massive object in the hydrodynamical simulation.

2.2 Insights from radial profiles

Throughout the initial collapse the halo structure is well approximated by ellipsoidal collapse models. We therefore explore radial profiles of various physical quantities to extract information about the galactic environment. The density is illustrated in Fig. 2, which is reasonably approximated by a broken power law over the range $r \in (10^{-3}, 10^3) \text{ pc}$. The break radius is due to the choice of the density resolution threshold, or equivalently, the limited resolution implies the pre-formation profile corresponds to roughly a dynamical time, as evaluated at the maximum resolved density, of $\sim 10 \text{ kyr}$ prior to the formation of the protostar. If the evolution proceeds under self-similar, isothermal collapse then the break in the profile will shift to smaller scales, eventually reaching the radius of the protostar (Abel et al. 2002; Becerra et al. 2015). We note that secondary infall and accretion results in a density distribution that is steeper than the $\rho \propto r^{-2}$ profile produced by violent relaxation. We find a power-law scaling of $\rho \propto r^{-7/3}$ in good agreement with Bertschinger (1985) where $\rho \propto r^{-9/4}$ and Wise et al. (2008) where $\rho \propto r^{-12/5}$, except in the core where the slope flattens off to $\rho \propto r^{-0.4}$ around $r \approx 0.3 \text{ pc}$. During the initial collapse and formation, the gas remains neutral with only a small abundance of free protons. Specifically, the ionization fraction, $x_{\text{H II}} \equiv n_{\text{H II}}/n_{\text{H}}$, is typically of order 10^{-5} to 10^{-3} depending on the density, such that $n_{\text{H II}} \sim 0.1 \text{ cm}^{-3} (r/10 \text{ pc})^{-5/3}$. As expected for direct collapse, the central region has access to at least $10^5 M_{\odot}$ of gas within a radius of $\approx 1.3 \text{ pc}$. More broadly, the enclosed baryonic mass is $M_{<r} \approx 4\pi \int_0^r \rho(r) r^2 dr$ (for 1D profiles), calculated explicitly as

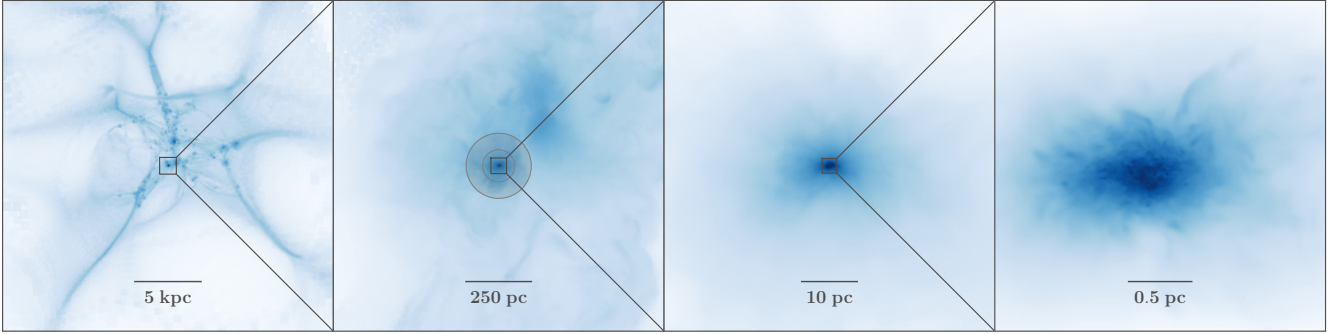


Figure 1. Projected gas density from an ab initio cosmological simulation, (Becerra et al. 2017), where primordial gas undergoes the direct collapse to a black hole (DCBH). The gas flows along filaments of dark matter that form a cosmic web structure in the early Universe. The panels illustrate the large-scale environment, host galaxy and the dense self-gravitating cloud where the DCBH forms at redshift $z \approx 11.6$, corresponding to 385 Myr after the big bang. For comparison, the $2.2' \times 2.2'$ field of view for the *JWST* is about 400 times larger in area than the left-hand panel. The circles in the second panel show the $0.032''$ and $0.065''$ pixel resolution of the NIRCcam instrument on board the *JWST* for the 2 and $4 \mu\text{m}$ channels, respectively.

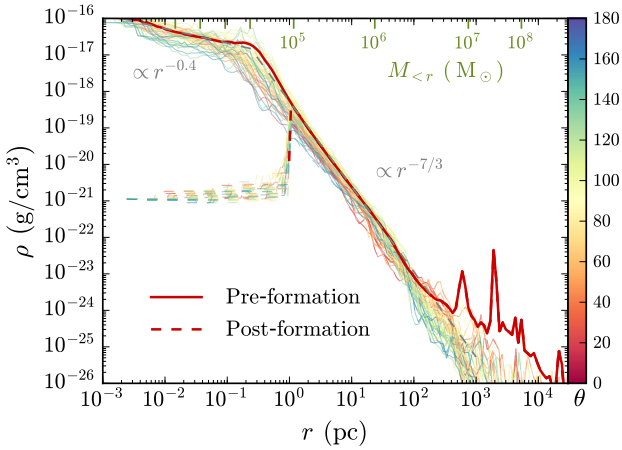


Figure 2. Radial density profile $\rho(r)$ for different lines of sight, which may be approximated as a broken power law separating the core and halo regions at $r \approx 0.3 \text{ pc}$. The $\rho \propto r^{-7/3}$ scaling is steeper than the $\rho \propto r^{-2}$ isothermal profile produced by violent relaxation. The solid curve corresponds to the initial collapse while the dotted curve has been evolved according to a massive sink particle prescription. The corresponding enclosed gas mass $M_{<r}$ is denoted by green markers at the top.

$M_{<r} \equiv \sum_{<r} \rho_i V_i$ where the sum is over all Voronoi cells within a radius r , and the subscript denotes cell quantities for density ρ_i and volume V_i . For convenience and completeness, in Table 1 we provide radial scaling relations for several relevant quantities, calculated as mass-weighted averages within shell volumes, i.e.

$$\langle q \rangle_{\text{shell}} \equiv \frac{\int q \rho dV}{\int \rho dV} \approx \frac{\sum q_i \rho_i V_i}{\sum \rho_i V_i}, \quad (1)$$

where the discretized version sums over all cells within each shell. Similarly, we obtain mass-weighted line of sight averages with

$$\langle q \rangle_{\text{LOS}} \equiv \frac{\int q \rho d\ell}{\int \rho d\ell} \approx \frac{\sum q_i \rho_i \Delta \ell_i}{\sum \rho_i \Delta \ell_i}, \quad (2)$$

where the integral is along radial rays within each shell and the summation is the discretized version calculated by ray tracing.

As seen in Fig. 3, the gas is experiencing both cosmologi-

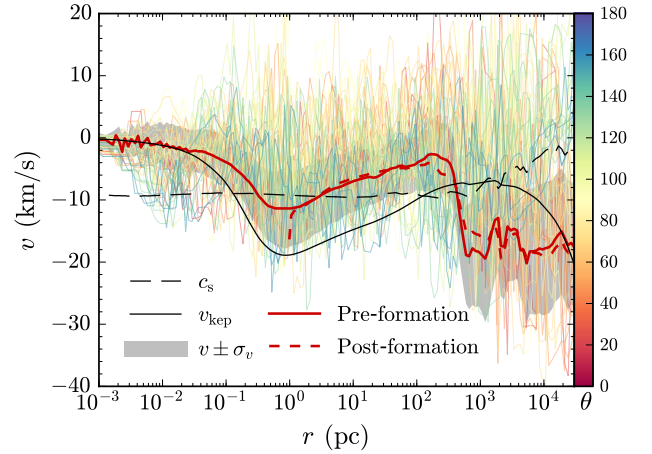


Figure 3. Radial velocity profile v_r for different sightlines. The relationship to the Keplerian velocity $v_{\text{kep}} \equiv \sqrt{GM_{<r}/r}$ (solid black curve) is approximately $|v_r| \approx v_{\text{kep}}/2$ within the virial radius and $|v_r| \approx 2v_{\text{kep}}$ beyond that due to cosmological inflow. The sound speed c_s (dashed black curve) is $\approx 9 - 9.5 \text{ km s}^{-1}$ throughout. Radial scaling relations are provided in Table 1.

cal inflow throughout the halo and collapse within the central region. To quantify this, we consider the mass accretion rate $\dot{M} \equiv -4\pi r^2 \rho v_r$, which has a maximum value of $2.35 M_{\odot} \text{ yr}^{-1}$ at 0.465 pc just outside the core radius. In Fig. 3, we also show the mass-weighted velocity along multiple sightlines and find a considerable scatter across different directions, as quantified by the velocity dispersion (grey region) in each shell as $\sigma_v \equiv (\langle v^2 \rangle - \langle v \rangle^2)^{1/2}$. Angular momentum does not appear to inhibit the inflow in this case. In particular, we calculate the Keplerian or rotational velocity as $v_{\text{kep}} \equiv \sqrt{GM_{<r}/r}$ (solid black curve) and find that $|v_r| \approx v_{\text{kep}}/2$ within the virial radius and $|v_r| \approx 2v_{\text{kep}}$ beyond, the latter is a reflection of cold gas inflow along the filaments. The associated Keplerian angular momentum is $j_{\text{kep}} = r v_{\text{kep}}$ and calculating the magnitude of the mass-weighted specific angular momentum demonstrates that $|j|/j_{\text{kep}} \approx 0.4 - 0.6$ throughout the halo except in the immediate vicinity of the collapsing region ($\lesssim 0.01 \text{ pc}$) where the role of angular momentum is less certain. In Fig. 3, we also show

Table 1. Radial scaling relations for various physical quantities calculated as mass weighted averages. Most of the profiles are reasonably approximated by a broken power law separated into regions I and II as $r \in (10^{-3}, r_{\text{I-II}})$ pc and $r \in (r_{\text{I-II}}, 10^3)$ pc, respectively, where $r_{\text{I-II}}$ is the radius connecting the regions. For convenience, the scalings are normalized according to values representative of the centre of each region, i.e. $r_{\text{I}} \equiv r/(0.05)$ pc and $r_{\text{II}} \equiv r/(10)$ pc. All relations are approximate fits to simulation data based on shell and line-of-sight averages described by equations (1) and (2). See the text for definitions and descriptions of all quantities.

Quantity	Units	Region I	Region II	$r_{\text{I-II}}$ [pc]
ρ	[g cm ⁻³]	$2.78 \times 10^{-17} r_{\text{I}}^{-0.4}$	$2.46 \times 10^{-21} r_{\text{II}}^{-7/3}$	0.24
n_{H}	[cm ⁻³]	$1.26 \times 10^7 r_{\text{I}}^{-0.4}$	$1.12 \times 10^3 r_{\text{II}}^{-7/3}$	0.24
$x_{\text{H II}}$	[1]	$1.15 \times 10^{-5} r_{\text{I}}^{-0.3}$	$1.15 \times 10^{-4} r_{\text{II}}^{2/3}$	0.18
$M_{<r}$	[M _⊙]	$214 r_{\text{I}}^{2.6}$	$5.10 \times 10^5 r_{\text{II}}^{2/3}$	0.45
\dot{M}	[M _⊙ /yr]	$0.0325 r_{\text{I}}^{2.3}$	$0.327 r_{\text{II}}^{-2/3}$	0.36
v_r	[km s ⁻¹]	$-2.47 r_{\text{I}}^{0.7}$	$-6.99 r_{\text{II}}^{-1/4}$	0.6
σ_v	[km s ⁻¹]	$3.83 r_{\text{I}}^{0.18}$	$4.94 r_{\text{II}}^{-0.1}$	0.82
v_{kep}	[km s ⁻¹]	$4.29 r_{\text{I}}^{0.8}$	$14.8 r_{\text{II}}^{-1/6}$	0.45
j_{kep}	[pc km s ⁻¹]	$0.215 r_{\text{I}}^{1.8}$	$148 r_{\text{II}}^{5/6}$	0.45
$ j /j_{\text{kep}}$	[1]	< 10	≈ 0.4 – 0.6	0.01
T	[K]	≈ 7000 – 8000	≈ 7000 – 8000	–
c_s	[km s ⁻¹]	≈ 9 – 9.5	≈ 9 – 9.5	–
t_{ff}	[Myr]	$0.0127 r_{\text{I}}^{0.2}$	$0.733 r_{\text{II}}^{7/6}$	0.45
λ_j	[pc]	$0.181 r_{\text{I}}^{0.2}$	$11.2 r_{\text{II}}^{7/6}$	0.42
$\lambda_j/2r$	[1]	$3.61 r_{\text{I}}^{-0.8}$	$1.12 r_{\text{II}}^{1/6}$	0.42
a_{grav}	[km s ⁻¹ Myr ⁻¹]	$413 r_{\text{I}}^{0.6}$	$38.1 r_{\text{II}}^{-1.1}$	0.38
a_{p}	[km s ⁻¹ Myr ⁻¹]	$536 r_{\text{I}}^{-1}$	$12.5 r_{\text{II}}^{-1}$	0.3
a_{ram}	[km s ⁻¹ Myr ⁻¹]	$92.2 r_{\text{I}}^{0.4}$	$1.08 r_{\text{II}}^{-3/2}$	0.32
$a_{\text{p}}/a_{\text{grav}}$	[1]	$1.30 r_{\text{I}}^{-1.6}$	$0.328 r_{\text{II}}^{0.1}$	0.15

the sound speed (dashed black curve) defined as $c_s \equiv \sqrt{\gamma k_B T / \mu}$, where in primordial gas the adiabatic index is $\gamma = 5/3$ and the mean molecular weight is $\mu \approx 1.22 m_{\text{H}}$. However, atomic line cooling efficiently regulates the temperature to $T \approx 7000 - 8000$ K, so the sound speed is also roughly constant at $c_s \approx 9 - 9.5$ km s⁻¹ throughout the halo.

Dynamical quantities are also of interest. We find short free-fall times within the core ($\approx 5 - 25$ kyr), rapidly rising beyond, such that $t_{\text{ff}} \approx \{15, 60, 775\}$ kyr at $r = \{0.1, 1, 10\}$ pc, respectively. Here, $t_{\text{ff}} \equiv \sqrt{3\pi/32G\bar{\rho}}$, where $\bar{\rho} \equiv 3M_{<r}/4\pi r^3$ is the average density within a given radius. To quantify the stability of the system we consider the Jeans length $\lambda_j \equiv \sqrt{15k_B T/4\pi G\mu\bar{\rho}} \sim t_{\text{ff}} c_s$. Interestingly, the ratio of the Jeans length to the diameter has a minimum value just outside the core radius, i.e. $\min(\lambda_j/2r) = 0.84$ at $r = 0.83$ pc, indicating that the break in the roughly isothermal scaling may be related to this instability length-scale. However, the break may also partially be a result of limited numerical resolution in the regions of highest density. Finally, outside the core both the gravitational and gas pressure acceleration components scale inversely with radius, $a \propto r^{-1}$. This is as expected for near-isothermal profiles in which the density profile $\rho \propto r^{-2}$ gives an enclosed mass of $M_{<r} \propto r$ so the acceleration is $a_{\text{grav}} \propto M_{<r}/r^2 \approx r^{-1}$. Furthermore, the gas pressure is roughly proportional to the density, i.e. thermal pressure $\sim \rho k_B T$ with constant temperature or ram pressure $\sim \rho \sigma^2$ with constant velocity dispersion, so the force is $a_{\text{p}} \propto d \log \rho / dr \approx r^{-1}$. The radial deceleration due to ram pressure, defined by $a_{\text{ram}} \equiv v_r \frac{dv_r}{dr}$, exhibits a steeper radial profile of $\propto r^{-3/2}$, but is about an order of magnitude smaller than the other forces. In general, the accelerations can have large variations across different

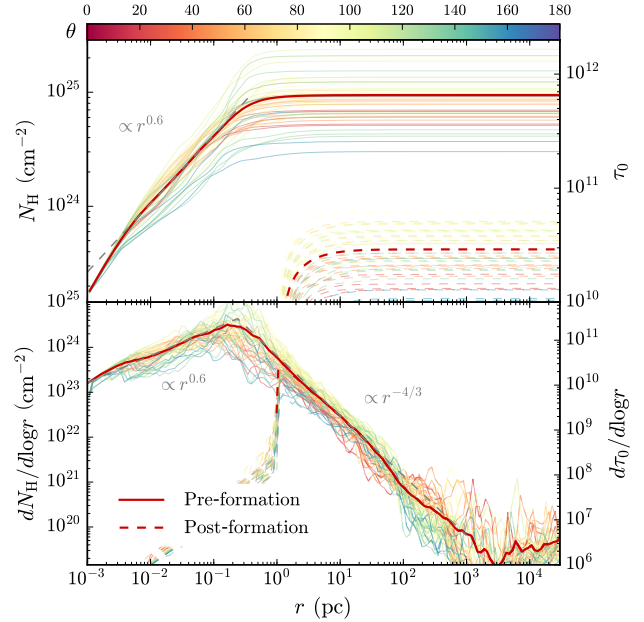


Figure 4. Radial column density of hydrogen, $N_{\text{H}} = \int_0^r n_{\text{H}} dl$ (upper panel) along with the local contribution estimated by $dN_{\text{H}}/d \log r = n_{\text{H}} r$ (lower panel). For convenience we also provide the corresponding Ly α optical depth at line centre $\tau_0 \approx N_{\text{H}} \sigma_0$ (isothermal gas), where the Ly α cross-section at line centre is $\sigma_0 = 5.9 \times 10^{-14} \text{ cm}^2 T_4^{-1/2}$. In such optically thick environments, Ly α photons emitted in the sub-parsec vicinity of the DCBH would be severely trapped and presumably destroyed by collisional de-excitation. However, this is mitigated by fewer scattering events once the gas becomes ionized.

sightlines, but gravity dominates the overall gas dynamics during the collapse stage.

3 IONIZING RADIATION

3.1 Neutral hydrogen column density

During the collapse phase the central region accumulates a significant amount of dense neutral gas. As seen in Fig. 4, the dominant contribution to the radially-integrated opacity is from the core, where the hydrogen column density is $N_{\text{H}}(r) \equiv \int_0^r n_{\text{H}} dl \sim 10^{25} \text{ cm}^{-2}$ and the optical depth for ionizing radiation is $\tau_{\text{ion}} \approx N_{\text{H}} \sigma_{\text{ion}} \gtrsim 10^7$ assuming $\sigma_{\text{ion}} \gtrsim 10^{-18} \text{ cm}^2$ near the 13.6 eV hydrogen ionization threshold. The variation along sightlines is roughly one order of magnitude with the minimum columns oriented along the poles of the angular momentum axis. Fig. 4 also shows the optical depth for Ly α resonant scattering at line centre, which is $\tau_0 \approx N_{\text{H}} \sigma_0$ in isothermal gas with a Ly α cross-section at line centre of $\sigma_0 = 5.9 \times 10^{-14} \text{ cm}^2 T_4^{-1/2}$, where $T_4 \equiv T/(10^4 \text{ K})$.

3.2 Expansion of the ionization front

During the formation of the central supermassive object, the high density implies that the ionization front is bounded within the dense sub-parsec core. However, as the black hole grows, at least three effects are likely to allow the ionization front to eventually break out of the core within a relatively short time. First, the number of ionizing photons increases rapidly; secondly, accretion removes gas ef-

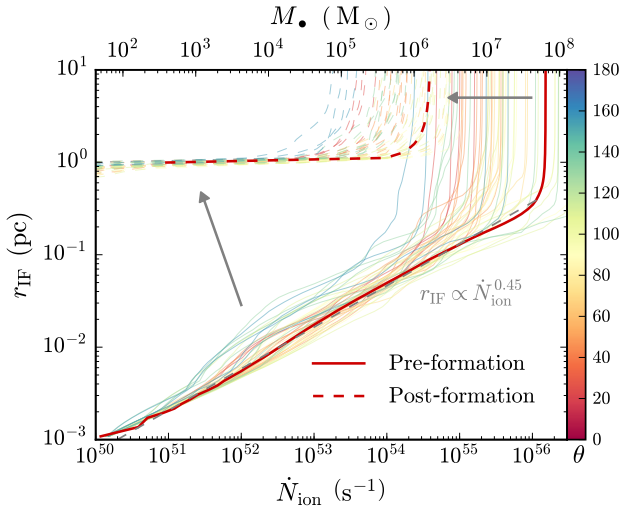


Figure 5. Estimated ionization front r_{IF} as a function of the strength of the ionizing source \dot{N}_{ion} , which is proportional to the black hole mass M_{\bullet} at roughly $\sim 10^{48} \text{ s}^{-1} M_{\odot}^{-1}$. The calculation is based on a Strömgen analysis in which we integrate along rays in the simulation – see equation (3) and the subsequent discussion. The threshold for breakout is one to two orders of magnitude lower in the polar directions. The arrows indicate the effect of accretion on the evolution of the H II region.

ficiently enough to lower the ionization rate threshold to ionize the core; and thirdly, dramatic photoheating of the gas leads to rapid expansion, facilitating ionization by lowering the density and recombination rate. Once the ionization front has extended beyond the core into the $\propto r^{-7/3}$ profile, it quickly outruns the rest of the halo in approximately the light crossing time. We estimate the breakout to occur on the order of $\lesssim 10^5$ yr, which corresponds to the sound crossing time for the core.

To analyse the expansion of the ionization front we consider an equilibrium model in which recombinations balance ionizations within a Strömgen sphere. The number of ionizing photons per unit time emitted from the source needed to produce an ionized region of radius r_{IF} based on the density in the simulation is

$$\dot{N}_{\text{ion}} \approx 4\pi \int_0^{r_{\text{IF}}} \alpha_{\text{B}} n_{\text{H}}^2 r^2 dr, \quad (3)$$

where $\alpha_{\text{B}} = 2.59 \times 10^{-13} T_4^{-0.7} \text{ cm}^3 \text{ s}^{-1}$ is the effective Case B recombination coefficient (Osterbrock & Ferland 2006). This analysis is valid until dynamical processes kick in (e.g. accretion and radiative feedback), because the recombination time, $t_{\text{rec}} \sim 1/n_{\text{H}}\alpha_{\text{B}} \lesssim 1$ yr, is much shorter than the sound crossing time, $t_{\text{s}} \equiv r/c_{\text{s}} \approx 10^5$ yr ($r/1$ pc). The main goal of this paper is to determine the impact of Ly α radiation pressure in the vicinity of a DCBH. However, the development of the H II region will significantly modify the Ly α radiative transfer. Therefore, we consider how the full 3D ionization structure evolves in time. Even though the density profile is roughly spherically symmetric, the column density can differ by an order of magnitude between sightlines (compare Figs 1, 2 and 4). Fig. 5 demonstrates this effect by exhibiting the extent of the ionization front as a function of source ionization rate based on equation (3). The rate threshold to blow pockets out of the core is one to two orders of magnitude lower in the polar directions. Ultimately, the threshold is overcome for a significant solid angle as the accretion and intensifying source lead to an evolving system, as indicated by the arrows in Fig. 5. The rate of ionizing photons is proportional

to the black hole mass, although the details depend on the specific SED. To simplify the calculation, we assume a blackbody source emitting at the Eddington luminosity, $L_{\text{Edd}} = 4\pi GM_{\bullet} m_{\text{H}} c / \sigma_{\text{T}}$, with an effective temperature of $T_{\text{eff}} = 10^5$ K. Thus,

$$\begin{aligned} \dot{N}_{\text{ion}} &= \frac{\pi L_{\text{Edd}}}{\sigma_{\text{SB}} T_{\text{eff}}^4} \int_{\nu_{\text{min}}}^{\infty} \frac{B_{\nu}}{h\nu} d\nu \\ &\approx 2.37 \times 10^{54} \text{ s}^{-1} \left(\frac{M_{\bullet}}{10^6 M_{\odot}} \right), \end{aligned} \quad (4)$$

where σ_{SB} is the Stefan–Boltzmann constant, B_{ν} the Planck function, and $h\nu_{\text{min}} = 13.6$ eV. However, a harder (softer) SED or more (less) efficient source produces more (fewer) ionizing photons per unit time, implying an uncertainty in the constant of proportionality of at least a factor of a few (Bolton et al. 2010; Yue et al. 2013).

Finally, we briefly explain why the halo is ionized so quickly once the ionization rate threshold is reached. We first approximate equation (3) by $\dot{N}_{\text{ion}} \propto n_{\text{H,rms}}^2 r_{\text{IF}}^3$, where the rms number density within the ionized region is $n_{\text{H,rms}} \equiv (3 r_{\text{IF}}^{-3} \int_0^{r_{\text{IF}}} n_{\text{H}}^2 r^2 dr)^{1/2}$. In our case the power law in the core is observed to be $n_{\text{H}} \propto r^{-0.4}$, which is preserved when calculating the rms density. This explains the origin of the scaling in the central region of Fig. 5, where we find $\dot{N}_{\text{ion}} \propto (r_{\text{IF}}^{-0.4})^2 r_{\text{IF}}^3 = r_{\text{IF}}^{2.2}$, or an inverted relation of $r_{\text{IF}} \propto \dot{N}_{\text{ion}}^{0.45}$. Outside the core the profile falls off rapidly and the rms density integral is dominated by the contribution from the core, i.e. $\int_0^{r_{\text{IF}}} n_{\text{H}}^2 r^2 dr \rightarrow \text{constant}$. Therefore, the rms scaling becomes $n_{\text{H,rms}} \propto r^{-3/2}$ and the required rate of ionizing photons saturates outside the core because $\dot{N}_{\text{ion}} \propto n_{\text{H,rms}}^2 r_{\text{IF}}^3 \approx \text{const.}$

4 LYMAN-ALPHA TRAPPING

4.1 Sub-parsec optical depth

During DCBH assembly the optical depth for Ly α photons at line centre can be significantly higher than what is typically described as extremely optically thick, conventionally defined by the condition $a\tau_0 \gtrsim 1000$ or equivalently $\tau_0 \gtrsim 2 \times 10^6 T_4^{1/2}$ (Adams 1972). Here, the damping parameter $a \equiv \Delta\nu_{\text{L}}/2\Delta\nu_{\text{D}}$, is half the ratio of the natural line width to the thermally broadened Doppler width. To distinguish between the broad range of environments we term even higher opacity regimes as ‘hyper-extreme’, as is the case for DCBH formation where $\tau_0 \sim 10^{12}$ (see Fig. 4). However, the escape of Ly α photons at hyper-extreme optical depths will be regulated by photoionization, two-photon emission, velocity gradients, dust absorption and 3D effects such as gas clumping, rotation, filamentary structure, holes or anisotropic emission. These effects are not independent of each other. For example, even at high densities collisional de-excitation becomes inefficient if the average number of scatterings remains lower than a certain threshold (Dijkstra et al. 2016b). Which effects are most important to accurately model?

We first consider the nature of Ly α resonant scattering in extremely opaque media, which can be thought of as a diffusion process in both frequency and space (Adams 1972; Harrington 1973; Neufeld 1990). The frequency diffusion accounts for partially coherent scattering in the wings of the Ly α profile (Unno 1952; Hummer 1962), and reduces the mean number of scatterings from the strong $N_{\text{scat}} \propto \tau^2$ dependence under a spatial random walk to a nearly linear scaling $N_{\text{scat}} \propto \tau_0$ (Osterbrock 1962; Adams 1972). However, at these opacities the mean number of successive wing scatterings just before escape may still be described as a diffusion process at the effective wing optical depth, i.e. $N_{\text{scat,w}} = \tau_{\text{w}}^2 \approx (a\tau_0)^{2/3}/\pi \approx 19.25 (\tau_0/10^6)^{2/3} T_4^{-1/3}$ (Ahn et al.

2002), emphasizing the role of excursions to the wing in facilitating the propagation of Ly α photons. For additional details and discussion of Ly α radiative transfer see the review by Dijkstra (2014).

4.2 Two-photon decay

4.2.1 Number of scattering events

In this paper we adopt a value of $N_{\text{scat}} \approx 0.6 \tau_0$ based on numerical calculations in which Ly α photons are emitted in the centre of a uniform, static sphere (Dijkstra et al. 2006). This scenario provides a conservative upper limit on N_{scat} but should be close to the actual number for the following reasons. First, although the gas cloud is not static the infall velocity is comparable to the thermal velocity of the gas, and therefore only decreases N_{scat} by a small amount (Bonilha et al. 1979; Dijkstra et al. 2016a). Additionally, it has been shown that N_{scat} is independent of bulk velocity for uniform spheres undergoing solid-body rotation up to 300 km s^{-1} (Garavito-Camargo et al. 2014). Secondly, in reality the Ly α radiation is not centrally emitted, either due to radial dependence or offset with respect to the centre of mass of the cloud. However, this too has been shown to have only a minor effect on N_{scat} , reducing the estimate by a factor of approximately 1.4 – 2 for homogeneously distributed sources (Harrington 1973; Garavito-Camargo et al. 2014). Thirdly, 3D inhomogeneities may also lower the number of scatterings. Indeed, the column density may differ by an order of magnitude across sightlines (see Fig. 4). However, translating this to N_{scat} is non-trivial as multiple scattering tends to isotropize the radiation field. Even if Ly α photons are efficiently channeled towards low column pathways, in the DCBH scenario fragmentation is suppressed and the gas distribution remains fairly smooth, unlike multiphase models with clumpy sub-structures (Neufeld 1991; Gronke et al. 2017).

4.2.2 Escape fraction with de-excitation

We now estimate the impact of collisional de-excitation in the simulation. During Ly α scattering interactions with nearby protons can induce transitions of the form $2p \rightarrow 2s$. Once in the $2s$ -state, the excited atom returns to the ground state via two-photon decay. The probability that a Ly α photon is eliminated in this process per scattering event is

$$p_{\text{dest}} = \frac{n_p C_{ps}}{n_p C_{ps} + A_\alpha} \approx 2.83 \times 10^{-7} \left(\frac{n_p}{10^6 \text{ cm}^{-3}} \right), \quad (5)$$

where n_p is the number density of free protons, $A_\alpha = 6.25 \times 10^8 \text{ s}^{-1}$ is the Einstein-A coefficient of the Ly α transition and $C_{ps} = 1.77 \times 10^{-4} \text{ cm}^3 \text{ s}^{-1}$ is the collision strength, which has weak dependence on temperature (Seaton 1955; Dennison et al. 2005). The fraction of Ly α photons that is *not* destroyed after N_{scat} scattering events at constant density and temperature is (Dijkstra et al. 2016b)

$$f_{\text{esc}}^{2\gamma} = [1 - p_{\text{dest}}]^{N_{\text{scat}}} \approx 1 - N_{\text{scat}} p_{\text{dest}}, \quad (6)$$

where the second expression is valid when $p_{\text{dest}} \ll 1$. If we ignore helium ionizations then the free proton number density is $n_p \approx x_e n_{\text{H}}$, where x_e denotes the ionized fraction. Additionally, a static uniform sphere gives $N_{\text{scat}} \approx 0.6 \tau_0 \approx 3.28 \times 10^6 T_4^{-1/2} \left(\frac{1-x_e}{10^{-4}} \right) \left(\frac{n_{\text{H}}}{10^6 \text{ cm}^{-3}} \right) \left(\frac{R}{0.3 \text{ pc}} \right)$, where R is the radius of the high-density cloud. This implies a critical density for which Ly α photons do not escape ($f_{\text{esc}}^{2\gamma} \ll 1$) of

$$n_{\text{H,crit}} \approx 10^6 \text{ cm}^{-3} T_4^{1/4} \left(\frac{x_e(1-x_e)}{10^{-4}} \frac{R}{0.3 \text{ pc}} \right)^{-1/2}. \quad (7)$$

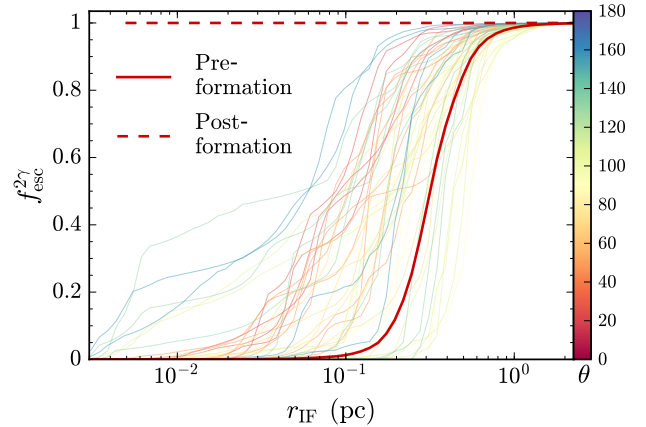


Figure 6. The escape fraction of Ly α photons accounting for collisional de-excitation that induces $2p \rightarrow 2s$ transitions converting Ly α into two-photon emission. This process renders escape impossible as long as the gas remains neutral. However, once the ionization front r_{IF} breaks out of the core around 0.3 pc, the number of scatterings decreases significantly. With a strong ionizing source, both the pre- and post-formation density profiles allow escape for photons emitted near the centre.

We also calculate $f_{\text{esc}}^{2\gamma}$ directly from the simulation data accounting for non-uniform conditions by taking the product from successive shells. The radial dependence is given by cumulative product within the region of interest

$$f_{\text{esc}}^{2\gamma} = \prod [1 - p_{\text{dest}}]^{\Delta N_{\text{scat}}}, \quad (8)$$

where $\Delta N_{\text{scat}} \approx 0.6 \Delta \tau_0$ denotes the contribution of each shell to the total number of scatterings. This shell-by-shell approximation is appropriate because additional scattering events take place under volume-weighted average conditions. The continuous version of equation (8) is derived from the geometric product integral

$$\begin{aligned} f_{\text{esc}}^{2\gamma} &= \exp \left[\int \ln(1 - p_{\text{dest}}) dN_{\text{scat}} \right] \\ &\approx \exp \left[-0.6 \int p_{\text{dest}} n_{\text{H}} \sigma_0 dr \right] \\ &\approx \exp \left[-\frac{3.1}{\text{pc}} \int \frac{x_e(1-x_e)}{10^{-4}} \left(\frac{n_{\text{H}}}{10^6 \text{ cm}^{-3}} \right)^2 T_4^{-1/2} dr \right]. \end{aligned} \quad (9)$$

The exponential behaviour leads to a sharp cut-off corresponding to a characteristic length-scale for destruction of Ly α photons via two-photon decay. The degree of ionization also affects the likelihood of escape. Fig. 6 shows the effect of a central ionizing source on the total $f_{\text{esc}}^{2\gamma}$, i.e. $r \gg r_{\text{vir}}$, as calculated from equation (8). We assume a constant ionization fraction of $x_e \approx 10^{-4}$ within the ionization front. Specifically, for $r < r_{\text{IF}}$ the number densities from the hydrodynamical simulation are modified as follows: $n_p \approx n_{\text{H}}$ and $n_{\text{H}} \approx x_e n_{\text{H}}$ in the calculations for p_{dest} and ΔN_{scat} , respectively. We have checked that the result is not sensitive to the exact value of x_e . If the core remains neutral then essentially no Ly α photons are able to escape the core. However, as the DCBH forms and ionizes the gas, collisional de-excitation no longer regulates the Ly α luminosity, even for central emission. Finally, we note that Ly α radiation pressure may still be an important source of feedback in such compact environments despite the reduced force multiplication due to two-photon decay.

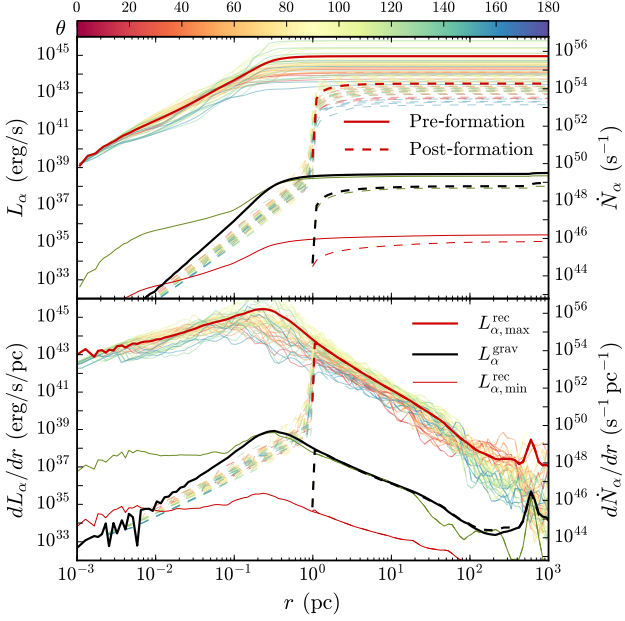


Figure 7. Radial dependence of the intrinsic Ly α emission, including the cumulative luminosity L_α (top panel) and its derivative dL_α/dr (bottom panel). The peak corresponds to the transition out of the core of the density profile. Ly α emission from recombinations in ionized (neutral) gas is illustrated by thick (thin) red curves, denoted by the subscript ‘max’ (‘min’) (see Table 2 for further details). Ly α cooling radiation from gravitational collapse is shown as the black curve. We also show the Ly α emission due to collisional excitation as the thin green line (see equation 15a of Cen 1992), which is comparable to our estimate for L_α^{grav} .

4.3 Intrinsic luminosity

During DCBH formation, excess thermal energy from the collapsing gas is efficiently radiated away via atomic line cooling with approximately $f_\alpha \sim 40\%$ of the release in gravitational binding energy being converted to Ly α emission (Dijkstra 2014). The gravitational potential energy is given by $dU = -GM_{<r}dm/r$, where the differential mass in spherical geometry is $dm = 4\pi r^2 \rho dr$. The radial dependence of the intrinsic Ly α luminosity then is

$$\frac{dL_\alpha^{\text{grav}}}{dr} = f_\alpha \frac{dU}{dr} = 4\pi f_\alpha G r \rho \dot{M}, \quad (10)$$

and the cumulative intrinsic Ly α luminosity is

$$L_\alpha^{\text{grav}} = 16\pi^2 f_\alpha G \int_0^R r^3 \rho^2 v_r dr. \quad (11)$$

In practice, we calculate the luminosity as the cumulative sum from discrete cells or shells according to

$$L_\alpha^{\text{grav}} = f_\alpha \sum \frac{GM}{r} \Delta m, \quad (12)$$

where gas must be infalling to contribute. The effects of dark matter are implicit in the gas density and velocity profiles. We note that Ly α cooling radiation arises from any physical mechanism that facilitates collisional excitation, collisional ionization, or recombination, e.g. shock heating, microturbulence, background radiation, etc. Such processes are indirectly included in our calculation of L_α^{grav} based on energy considerations and may be ignored once Ly α emission is dominated by black hole accretion and nebular sources.

Table 2. Radial scaling relations for the Ly α luminosity calculated by equations (12) and (13). The notation for the broken power law is the same as Table 1, i.e. $r_I \equiv r/(0.05 \text{ pc})$ and $r_{II} \equiv r/(10 \text{ pc})$. Calculations in fully ionized and mostly neutral gas are denoted by the subscripts ‘max’ and ‘min’, respectively. As in Table 1, the scalings are given as pre-formation profiles in order to retain information on sub-parsec scales. However, the pre-formation case cannot be ionized so the cumulative value serves as an upper limit. A more conservative value for the luminosity after ionization breakout is $L_{\alpha,\text{max}}^{\text{rec}} \approx 5 \times 10^{43} \text{ erg s}^{-1}$, corresponding to the ionized post-formation curve shown in Fig. 7.

Quantity	Units	Region I	Region II	r_{I-II} [pc]
$L_{\alpha,\text{max}}^{\text{rec}}$	[erg/s]	$1.16 \times 10^{43} r_I^{2.2}$	$\approx 9.0 \times 10^{44}$	0.36
L_α^{grav}	[erg/s]	$1.29 \times 10^{35} r_I^{3.9}$	$\approx 4.4 \times 10^{38}$	0.40
$L_{\alpha,\text{min}}^{\text{rec}}$	[erg/s]	$3.18 \times 10^{33} r_I^{1.6}$	$\approx 3.0 \times 10^{35}$	0.36
$\frac{d}{dr} L_{\alpha,\text{max}}^{\text{rec}}$	[erg/s/pc]	$4.70 \times 10^{44} r_I^{1.2}$	$1.33 \times 10^{41} r_{II}^{-8/3}$	0.23
$\frac{d}{dr} L_\alpha^{\text{grav}}$	[erg/s/pc]	$7.91 \times 10^{36} r_I^{2.9}$	$1.40 \times 10^{36} r_{II}^{-2}$	0.31
$\frac{d}{dr} L_{\alpha,\text{min}}^{\text{rec}}$	[erg/s/pc]	$8.76 \times 10^{34} r_I^{0.6}$	$1.85 \times 10^{33} r_{II}^{-4/3}$	0.26

After the formation of a collapsed central object, ionizing radiation from the accretion disc leads to the efficient production of Ly α photons via recombinations. The cumulative intrinsic Ly α luminosity due to recombinations is

$$L_\alpha^{\text{rec}} = 0.68 h\nu_\alpha \int_0^R 4\pi r^2 \alpha_B n_e n_p dr, \quad (13)$$

where $h\nu_\alpha = 10.2 \text{ eV}$ and the number densities n_e and n_p are for free electrons and protons (Dijkstra 2014). Fig. 7 illustrates the radial dependence of Ly α emission from gravitational collapse and recombinations. The peak of dL_α/dr corresponds to the transition out of the core of the density profile, i.e. the break in the power law. In the pre-formation phase Ly α cooling dominates at $L_\alpha^{\text{grav}} \approx 4.4 \times 10^{38} \text{ erg s}^{-1}$ while in post-formation recombinations from a central ionizing source can contribute as much as $L_\alpha^{\text{rec}} \sim 10^{45} \text{ erg s}^{-1}$ (see Table 2 for additional details).

However, the Ly α luminosity is also limited by the strength of the ionizing source. For concreteness, we relate the Ly α luminosity to the ionizing luminosity directly as

$$L_\alpha = \frac{3}{4} f_{\text{coll}} (1 - f_{\text{esc}}^{\text{ion}}) L_{\text{ion}}, \quad (14)$$

which accounts for the fact that harder ionizing spectra can boost the overall Ly α production per ionizing photon (Raiter et al. 2010; Dijkstra 2014). Here the ionizing luminosity is $L_{\text{ion}} \equiv \langle h\nu \rangle_{\text{ion}} \dot{N}_{\text{ion}} = \int_{\nu_{\text{min}}}^{\infty} L_\nu d\nu$ for a given source with $\nu_{\text{min}} = 13.6 \text{ eV}$. For reference, a blackbody source with an effective temperature of $T_{\text{eff}} = \{10^4, 10^5, 10^6\} \text{ K}$ has a mean energy per ionizing photon of $\langle h\nu \rangle_{\text{ion}} = \{14.57, 29.61, 233.9\} \text{ eV}$. The collisional parameter is defined as $f_{\text{coll}} \equiv (1 + 1.62 n_{\text{H},3}) / (1.56 + 1.78 n_{\text{H},3})$, where $n_{\text{H},3} \equiv n_{\text{H}} / (10^3 \text{ cm}^{-3})$ and is bounded by $0.64 < f_{\text{coll}} < 0.91$ in the low- and high-density limits, respectively. The factor of $(1 - f_{\text{esc}}^{\text{ion}})$ accounts for the escape of ionizing photons either from 3D effects or because the galaxy is ionized out into the intergalactic medium (IGM). If we combine equations (4) and (14) considering a blackbody with $T_{\text{eff}} = 10^5 \text{ K}$ emitting at the Eddington luminosity then the Ly α luminosity in the high-density, ionization-bound regime ($f_{\text{coll}} \approx 0.91$ and $f_{\text{esc}}^{\text{ion}} \ll 1$) is

$$L_\alpha = f_{\text{coll}} (1 - f_{\text{esc}}^{\text{ion}}) \frac{3\pi L_{\text{Edd}}}{4\sigma_{\text{SB}} T_{\text{eff}}^4} \int_{\nu_{\text{min}}}^{\infty} B_\nu d\nu \approx 7.67 \times 10^{43} \text{ erg s}^{-1} \left(\frac{M_\bullet}{10^6 M_\odot} \right), \quad (15)$$

or equivalently a rate of $\dot{N}_\alpha \approx 4.69 \times 10^{54} \text{ s}^{-1} (M_\bullet/10^6 M_\odot)$. In this case, the standard factor of 0.68 Ly α photons per ionizing photon is increased to $f_{\text{coll}}(h\nu)_{\text{ion}}/(13.6 \text{ eV}) \approx 2$. For comparison, higher effective temperatures or harder SEDs asymptotically approach the maximal Eddington-limited values of $L_{\alpha, \text{Edd}} \approx 8.58 \times 10^{43} \text{ erg s}^{-1} (M_\bullet/10^6 M_\odot)$ and $\dot{N}_{\alpha, \text{Edd}} \approx 5.25 \times 10^{54} \text{ s}^{-1} (M_\bullet/10^6 M_\odot)$.

We note that such efficient conversion to Ly α emission assumes a low escape fraction, which may not be the case for long mean free path high energy photons. A more self-consistent calculation would perform multi-wavelength ionizing radiative transfer directly from the SED, which will be done in future 3D RHD simulations of DCBH growth. Still, X-ray feedback may have important consequences for Ly α transport, which is sensitive to the ionization state and dynamical evolution of the gas. For example, in neutral gas a harder spectrum leads to a higher residual ionized fraction due to X-ray heating (Dijkstra et al. 2016b), while in ionized gas the longer mean free path implies a higher residual neutral fraction, which can increase the efficiency of Ly α driven winds (Smith et al. 2016). In the following subsection we account for some of the uncertainty regarding the ionizing source by varying $x_{\text{H I}} \equiv n_{\text{H I}}/n_{\text{H}}$. Furthermore, the post-processing analysis allows for luminosity rescaling given a particular SED. Therefore, we may meaningfully refer to both direct emission properties, such as \dot{N}_α , and model dependent quantities, such as M_\bullet .

4.4 Ly α radiative transfer simulations

The MCRT post-processing methodology that enables accurate Ly α radiation pressure calculations with the Cosmic Ly α Transfer code (COLT) is described in detail by Smith et al. (2015, 2017b). In particular, we employ Monte Carlo estimators based on the traversed opacity for continuous momentum deposition to reduce noise in regions with fewer scatterings. In order to maintain the spatial resolution of the simulation, we have extended the capabilities of COLT to run natively on unstructured mesh data, i.e. the Voronoi tessellation of points. In fact, COLT is able to perform Ly α radiative transfer with any particle-based data under the interpretation of a Voronoi tessellation, which can be efficiently and robustly constructed with preexisting software such as the Computational Geometry Algorithms Library (The CGAL Project 2017). Implementing ray tracing and other algorithms in this geometry follows standard techniques (e.g. Springel 2010), which have been carefully tested and optimized for Ly α radiative transfer.

4.4.1 Dynamical impact

Ly α radiation pressure may contribute alongside other forms of feedback to impose restrictions on the maximum mass of the seed black hole. If Ly α feedback is able to overcome gravity and the momentum of the inflowing gas, then the resulting outflow could signal an end to the assembly process. In Fig. 8, we illustrate the relative dynamical importance of Ly α radiation pressure compared to gravity. In the limit of a central, compact source the Ly α radiation field can significantly overwhelm gravity within the core. Specifically, in the notation of Table 1 we find the radial acceleration is $a_\alpha \sim \{10^{6-8} r_{\text{I}}^{-2.5}, 10^{1-3} r_{\text{II}}^{-1.8}\} \text{ km s}^{-1} \text{ Myr}^{-1} (M_\bullet/10^6 M_\odot)$ in regions I and II connecting at $r_{\text{I-II}} \sim 0.5 \text{ pc}$, with the coefficient range arising from different ionization fractions. However, for an extended source distributed according to the recombination rate (see L_α^{rec} in Fig. 7), Ly α trapping is reduced in the core, while

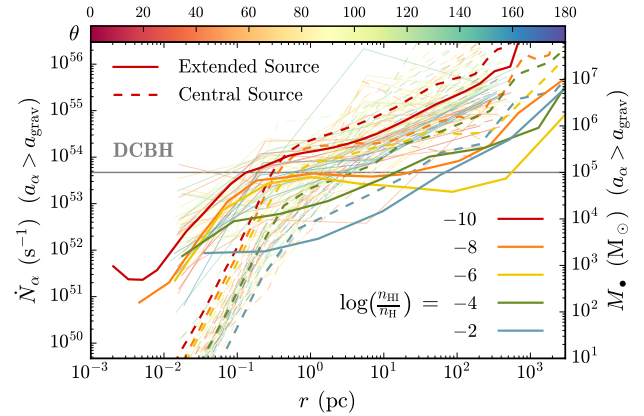


Figure 8. The total Ly α emission rate \dot{N}_α necessary for Ly α radiation pressure to overcome gravitational acceleration as a function of radius. Results are shown for the pre-formation scenario with varying degrees of ionization, $x_{\text{H I}} \equiv n_{\text{H I}}/n_{\text{H}}$, which strongly affects the optical depth for Ly α photons. Sightline dependence converges slowly and is only shown for the $\log x_{\text{H I}} = -10$ case to have fewer overlapping curves. We differentiate between a central source and extended emission from recombinations (see L_α^{rec} in Fig. 7). For similar luminosities, central emission has a greater impact within the core while the extended case more easily affects gas outside the core.

still having an impact. Interestingly, extended emission actually enhances the force outside the core because the Ly α photons have not diffused as far into the wings as in the central, bottled up scenario. For this same reason, we predict post-formation scenarios with reduced density in the core may allow Ly α radiation pressure to act on greater distances for similar luminosities, although we do not simulate this here. Overall, we expect Ly α feedback and gas pressure to contribute to the formation of galactic winds in response to the newly formed DCBH, given the typical mass range is $M_\bullet \sim 10^{4-6} M_\odot$. In the case that the core remains ionization bounded or two-photon decay destroys Ly α photons, the extent of Ly α feedback will be limited to within the core. However, considering the low threshold to affect the gas in these regions Ly α trapping should eventually be explored in fully coupled 3D RHD simulations. Despite the considerable uncertainty in the interpretation of our results, the post-processing analysis is indicative of the complexity and computational requirements to fully determine the dynamical impact of Ly α radiation pressure.

4.4.2 Escape properties

We now consider the characteristics of the intrinsic escape of Ly α photons during DCBH assembly. A single scattering with neutral hydrogen far from the source removes Ly α photons from the line of sight, so to first order all flux blueward of $\Delta\nu \lesssim 100 \text{ km s}^{-1}$ is eliminated. However, for simplicity we do not extrapolate to observed signatures based on IGM transmission. Instead we focus on the effects of the 3D geometry. Fig. 9 shows three basic parameters of the emergent line profiles for different values of $x_{\text{H I}} \equiv n_{\text{H I}}/n_{\text{H}}$ with either central or extended emission.

(i) The top panel demonstrates the strong effect of residual opacity on the velocity offset of the blue and red peaks, $\Delta\nu_{\text{peak}}$. Depending on the ionization state, the peaks are likely to emerge with a velocity offset and FWHM of $\sim 10^{2-3} \text{ km s}^{-1}$. Another interesting feature is the angular dependence of the peak location, dominated

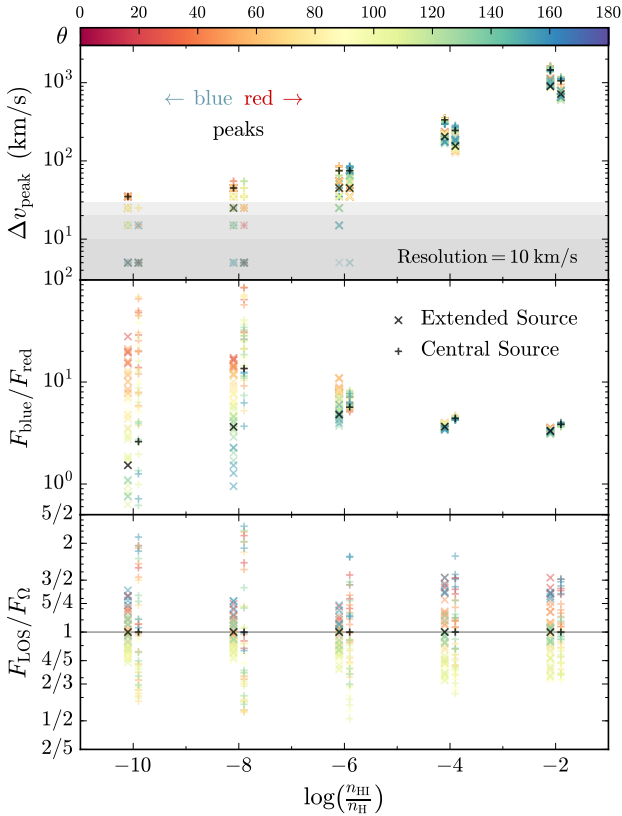


Figure 9. $\text{Ly}\alpha$ escape properties for different degrees of ionization, $x_{\text{H I}} \equiv n_{\text{H I}}/n_{\text{H}}$, including the velocity offset of the blue and red peaks, Δv_{peak} , flux ratio of the blue and red peaks, $F_{\text{blue}}/F_{\text{red}}$, and the angular dependence of the escaping bolometric flux compared to isotropic emission, $F_{\text{LOS}}/F_{\Omega}$. See the text for a discussion. Simulations with central and extended sources are denoted by ‘+’ and ‘x’ markers, respectively. Horizontal offsets have been applied in order to avoid confusion from overlapping data. Note that in the top panel the left and right points denote the blue and red peaks, respectively.

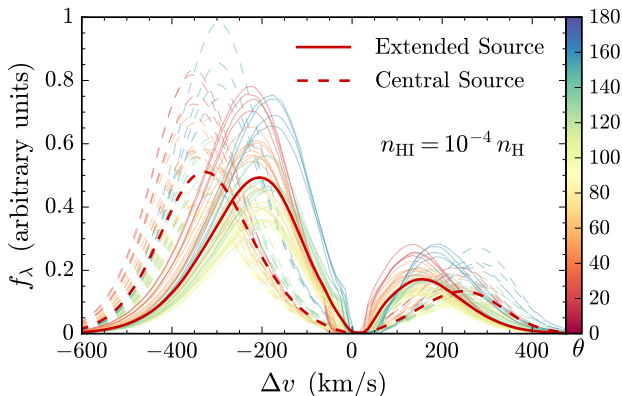


Figure 10. Line-of-sight $\text{Ly}\alpha$ flux as a function of Doppler velocity $\Delta v = c\Delta\lambda/\lambda$ for the case of an ionization fraction of $x_{\text{H I}} \equiv n_{\text{H I}}/n_{\text{H}} = 10^{-4}$. The main features include the enhancement of the blue peak due to gas infall, enhancement in the polar directions of the rotation axis, and the lower effective optical depth for extended emission compared to a central source.

by a dipole-like Doppler shift of $\Delta(\Delta v_{\text{peak}}) \approx \pm v_{\text{sys}} \approx \pm 24 \text{ km s}^{-1}$ due to the systemic velocity of the source with respect to the centre of mass, in addition to random velocity dispersions. Overall, the blue peak has a larger absolute velocity offset than the red peak, i.e. $|\Delta v_{\text{blue}}| > |\Delta v_{\text{red}}|$, and the peak separation has little variation across sightlines, i.e. $|\Delta v_{\text{blue}}| + |\Delta v_{\text{red}}| \approx \text{constant}$.

(ii) The middle panel shows the directional dependence of the blue to red flux ratio, $F_{\text{blue}}/F_{\text{red}}$. In the collapsing scenario, the blue peak dominates by a factor of a few with significant angular dependence in the optically thin limit, while converging to a factor of a few in the high-opacity limit. We also note that an extended source results in a more balanced profile (lower ratio) than a central source.

(iii) The lower panel illustrates the line-of-sight bolometric $\text{Ly}\alpha$ flux, F_{LOS} , compared to the isotropic case of $F_{\Omega} \equiv L_{\alpha}/(4\pi d_L^2)$, where d_L denotes the luminosity distance. Due to the ellipsoidal or thick-disc geometry (e.g. Lodato & Natarajan 2006), we find beaming along both directions of the angular momentum axis by a factor of a few compared to edge-on sightlines. It is important to note that the excess is less pronounced for extended emission than for a central source, although the difference may not matter in the optically thick limit.

Additional insights regarding the escape of $\text{Ly}\alpha$ photons in 3D DCBH environments are available upon close examination of the line profile of a single simulation. We choose the case of $x_{\text{H I}} = 10^{-4}$ and show the angular-dependence of the emergent flux density and bolometric flux in Fig. 10. All of the profiles show an enhancement of the blue peak due to gas infall, such that $F_{\text{blue}}/F_{\text{red}} \approx 4$. The line-of-sight flux is also noticeably enhanced by at least a factor of two along either direction of the rotation axis. Also, for a given simulation the locations of the blue and red peaks varies by approximately 50 km s^{-1} across different sightlines due to a systemic dipole velocity shift. The absolute peak separation is about 1.5 times smaller for the extended emission compared to the central source due to the lower effective optical depth. The shape of the profile is also noticeably different because each photon is emitted in distinct regions with unique pathways to escape. Interestingly, the more realistic recombination emission setup produces a more skewed or less symmetric line, similar to the observed profiles of many $\text{Ly}\alpha$ emitting galaxies (e.g. Rivera-Thorsen et al. 2015).

5 COMPTON SCATTERING

5.1 Initial stage

Before the H II region develops, the number density of free electrons is too low for significant Compton scattering. We calculate a lower limit for the Thomson optical depth of $\tau_{\text{T}} = N_e \sigma_{\text{T}} \gtrsim 10^{-5}$. Therefore, if the DCBH environment becomes optically thick to Compton scattering it is in response to ionizing radiation emitted from the newly formed black hole. However, as discussed previously, we do expect the gas to become ionized so the opacity calculated from the pre- and post-formation electron column densities will rise and has the potential to eventually rise to $\tau_{\text{T}} \gtrsim 1$ with the growth of the DCBH, rendering the emitting region Compton-thick.

5.2 Upper limits

Fig. 11 illustrates the effect of the ionization front radius r_{IF} on the cumulative optical depth to Compton scattering. Although we do not follow the hydrodynamical evolution beyond the initial formation, our extrapolation indicates that DCBH environments become

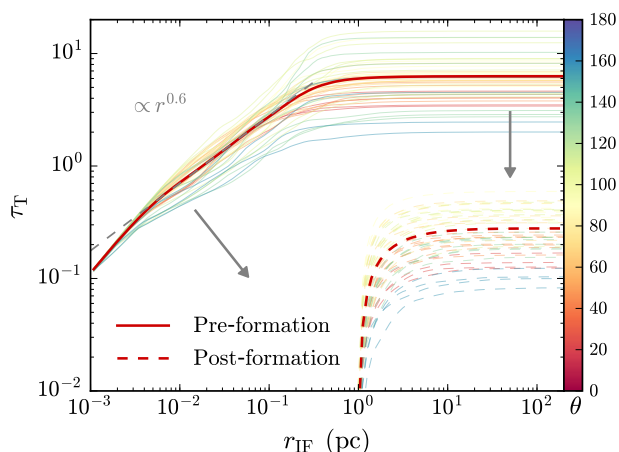


Figure 11. The optical depth to Compton scattering $\tau_T \sim N_H \sigma_T$ as a function of the extent of the ionization front r_{IF} . Even in the post-formation case the effect is at least marginally important for many sightlines ($\tau_T \sim 1$), and may need to be taken into account in hydrodynamical simulations.

Compton-thick for a significant fraction of sightlines. 1D RHD simulations combined with spectral synthesis modelling have already been carried out by Pacucci et al. (2015b) (see also Yue et al. 2013). They found that Compton-thickness does indeed occur, persisting for about 120 Myr under their standard accretion scenario. Furthermore, the emerging spectrum is strongly affected by the hydrogen column density as photons shortward of the Ly α line are reprocessed to lower energies. Thus, the predicted spectral signature of DCBHs exhibits characteristic non-thermal emission in the observed infrared and X-ray bands. The conditions for Compton-thickness still need to be explored with 3D ab initio simulations, including self-consistent buildup of the H II region and all relevant forms of radiative feedback.

An additional consideration is whether ongoing accretion is able to replenish the gas supply after the rapid formation of a central massive object. If runaway collapse efficiently evacuates the central parsec region, the replacement time is approximately $t_{acc} \approx M_{cr}/\dot{M} \gtrsim 72.3 \text{ kyr} (r/\text{pc})^{4/3}$, which is longer than the dynamical time by a factor of $t_{acc}/t_{ff} \gtrsim 1.45 (r/\text{pc})^{1/6}$. However, an extrapolation in time suggests that gas is not flowing into the core fast enough to maintain Compton-thickness indefinitely. At some point, the combination of decreasing column density and increasing radiation pressure dramatically alters the environment, leading to sub-Eddington black hole growth.

We emphasize that rapid evacuation of the central gas during the assembly of the initial seed black hole may reduce the post-formation accretion rates. For example, Pacucci et al. (2015a) suggest that super-Eddington accretion can occur for extended periods ($\gtrsim 100$ Myr), however, a lower ambient density could imply an earlier transition to feedback-limited growth rates. On the other hand, the authors also point out that a radiatively inefficient slim disc mode of accretion could allow for sub-Eddington luminosities and super-Eddington rates. Either way, 3D radiation hydrodynamics with ionizing and Ly α feedback in (near) Compton-thick settings may moderate extreme hyper-Eddington accretion in the aftermath of direct collapse.

6 SUMMARY AND CONCLUSIONS

We have explored the impact of radiative feedback on the assembly environments of direct collapse black holes. The main focus has been to apply a Monte Carlo Ly α radiative transfer code to calculate the pressure exerted by Ly α photons on the surrounding gas. Previous applications of this method have been limited to 1D geometries, either in the context of the expanding shell model (Dijkstra & Loeb 2008), or coupled to a spherically symmetric hydrodynamics code (Smith et al. 2017b). In this work, we have performed an exploratory post-processing analysis of the high-resolution ab initio cosmological simulation of Becerra et al. (2017). We found that Ly α radiation pressure is likely important in shaping the environment surrounding newly formed DCBHs. Therefore, 3D Ly α radiation hydrodynamics will be crucial to incorporate in future DCBH simulations, alongside accurate ionizing radiative transfer and Compton scattering as discussed above.

Our results confirm previous predictions that Ly α radiation can have a dynamical impact in realistic astrophysical settings, beyond its role as a probe of (inter)stellar and (inter)galactic properties. Still, determining the exact role of Ly α photon trapping is challenging both theoretically and observationally. For example, the Monte Carlo method is computationally demanding in extremely optically thick environments and great care must be taken to ensure convergence at every stage in fully coupled RHD simulations. However, more efficient algorithms and hardware will eventually make such calculations feasible. Additionally, upcoming observations with the *JWST* and other facilities extending our view of the high-redshift frontier will help guide and motivate simulations to better understand newly discovered phenomena. Still, our models robustly predict intense Ly α radiation pressure within the sub-parsec region. Certain configurations may extend the influence of Ly α feedback out to ~ 100 pc, although the quantitative details are likely sensitive to a number of environmental factors including photoionization, two-photon decay, velocity gradients, dust absorption and geometrical effects.

Details regarding the impact of Ly α feedback in the direct collapse scenario will remain uncertain until fully cosmological, on-the-fly simulations are available. Still, Ly α trapping likely induces thermal effects via less efficient cooling, chemical effects via photodetachment or photodissociation, and kinematic effects via direct momentum transfer. The thermal impact has recently been revisited by Ge & Wise (2017), who perform time-dependent Ly α radiative transfer on radially averaged profiles during the initial collapse of massive black hole seeds. Similar to Spaans & Silk (2006), the equation of state for gas at moderate densities ($n \sim 10^4 - 10^5$) could potentially have γ as high as 4/3, which would briefly affect the Jeans mass and reduce fragmentation. Ge & Wise (2017) claim a 50 000 K envelope forms at a radius of ~ 1 pc. However, the core still maintains near-isothermal collapse as cooling proceeds via other atomic hydrogen transitions and two-photon emission (e.g. Omukai 2001; Schleicher et al. 2010). Our work based on the simulation of Becerra et al. (2017) already includes an approximate prescription for Ly α trapping in this phase. Thus, we focus our investigation on the longer-term dynamical impact of Ly α radiation pressure once the massive object has formed. The importance of Ly α feedback during DCBH assembly seems fairly robust, however, fully coupled 3D calculations may be necessary for a self-consistent, higher order description. Of course, fundamental insights about Ly α radiative transfer can guide our understanding. For example, a static cloud of constant density has an approximate temperature dependence for the trapping time of

$t_{\text{trap}}/t_{\text{light}} \sim (\alpha\tau_0)^{1/3} \propto T^{-1/3}$ (Adams 1975), and the characteristic escape frequency changes as $\Delta\nu_{\text{peak}} = x_{\text{peak}}\nu_{\text{th}} \propto T^{1/6}$, where $x_{\text{peak}} \sim (\alpha\tau_0)^{1/3}$ and $\nu_{\text{th}} \propto T^{1/2}$ (e.g. Smith et al. 2015). Therefore, in the context of fully coupled simulations, we expect our results to be modified by other environmental factors, such as the rapid development of low-column pockets to facilitate the escape of Ly α photons.

Ly α trapping may also have an effect on other observational signatures. For example, additional radiation pressure provides negative feedback, making it more difficult for gas to reach the source, thereby regulating the black hole mass and luminosity $\propto \dot{M}_*$. The emerging SED is also indirectly related to Ly α processes as additional feedback may destroy the Compton-thickness property and excess two-photon emission earlier than expected. Ly α photons may also affect chemical processes via the photodetachment of ions and molecules. Finally, Ly α spectroscopy with next-generation observatories may provide further insights into high- z galaxies and radiative transfer effects, such as the presence (absence) of outflowing gas. In future studies it may be worth revisiting Ly α radiation pressure in the context of other environments as well. Ly α coupling is likely sub-dominant in simulations of massive star formation, including Population III stars (McKee & Tan 2008; Stacy et al. 2012), and galactic winds caused by AGN, starbursts and supernovae (Haehnelt 1995). However, there may be aspects in which these systems can still be dynamically influenced by Ly α trapping due to a radial scaling steeper than free-streaming, $d \log a_\alpha / d \log r < -2$, from force multiplication in the diffusion limit (Dijkstra & Loeb 2008; Smith et al. 2017b). In any case, Ly α photons are crucial in shaping conditions in the early Universe, and in allowing us to probe them.

ACKNOWLEDGEMENTS

This material is based upon work supported by a National Science Foundation Graduate Research Fellowship for AS. VB acknowledges support from NSF grant AST-1413501. We thank Benny Tsang for insightful discussions. We thank the anonymous referee for the prompt and constructive comments that improved the content of this paper. The authors acknowledge the Texas Advanced Computing Center (TACC) at the University of Texas at Austin for providing HPC resources.

REFERENCES

- Abel T., Bryan G. L., Norman M. L., 2002, *Science*, 295, 93
- Adams T. F., 1972, *ApJ*, 174, 439
- Adams T. F., 1975, *ApJ*, 201, 350
- Agarwal B., Khochfar S., 2015, *MNRAS*, 446, 160
- Agarwal B., Khochfar S., Johnson J. L., Neistein E., Dalla Vecchia C., Livio M., 2012, *MNRAS*, 425, 2854
- Agarwal B., Dalla Vecchia C., Johnson J. L., Khochfar S., Paardekooper J.-P., 2014, *MNRAS*, 443, 648
- Agarwal B., Johnson J. L., Zackrisson E., Labbe I., van den Bosch F. C., Natarajan P., Khochfar S., 2016, *MNRAS*, 460, 4003
- Agarwal B., Johnson J. L., Khochfar S., Pellegrini E., Rydberg C.-E., Klessen R. S., Oesch P., 2017, *MNRAS*, 469, 231
- Ahn S.-H., Lee H.-W., Lee H. M., 2002, *ApJ*, 567, 922
- Becerra F., Greif T. H., Springel V., Hernquist L. E., 2015, *MNRAS*, 446, 2380
- Becerra F., Marinacci F., Inayoshi K., Bromm V., Hernquist L. E., 2017, preprint (arXiv:1702.03941)
- Begelman M. C., Volonteri M., Rees M. J., 2006, *MNRAS*, 370, 289
- Behrens C., Dijkstra M., Niemeyer J. C., 2014, *A&A*, 563, A77
- Bertschinger E., 1985, *ApJS*, 58, 39
- Bolton J. S., Becker G. D., Wyithe J. S. B., Haehnelt M. G., Sargent W. L. W., 2010, *MNRAS*, 406, 612
- Bonilha J. R. M., Ferch R., Salpeter E. E., Slater G., Noerdlinger P. D., 1979, *ApJ*, 233, 649
- Bowler R. A. A., McLure R. J., Dunlop J. S., McLeod D. J., Stanway E. R., Eldridge J. J., Jarvis M. J., 2017, *MNRAS*, 469, 448
- Bromm V., Loeb A., 2003, *ApJ*, 596, 34
- Bromm V., Yoshida N., 2011, *ARA&A*, 49, 373
- Cappelluti N., et al., 2013, *ApJ*, 769, 68
- Cen R., 1992, *ApJS*, 78, 341
- Dayal P., Choudhury T. R., Pacucci F., Bromm V., 2017, *MNRAS*, preprint (arXiv:1705.00632)
- Dennison B., Turner B. E., Minter A. H., 2005, *ApJ*, 633, 309
- Dijkstra M., 2014, *Publ. Astron. Soc. Australia*, 31, e040
- Dijkstra M., Loeb A., 2008, *MNRAS*, 391, 457
- Dijkstra M., Loeb A., 2009, *MNRAS*, 396, 377
- Dijkstra M., Haiman Z., Spaans M., 2006, *ApJ*, 649, 14
- Dijkstra M., Sethi S., Loeb A., 2016a, *ApJ*, 820, 10
- Dijkstra M., Gronke M., Sobral D., 2016b, *ApJ*, 823, 74
- Fan X., et al., 2006, *AJ*, 131, 1203
- Gallerani S., Fan X., Maiolino R., Pacucci F., 2017, *Publ. Astron. Soc. Australia*, 34, e022
- Garavito-Camargo J. N., Forero-Romero J. E., Dijkstra M., 2014, *ApJ*, 795, 120
- Ge Q., Wise J., 2017, *MNRAS*, preprint (arXiv:1706.01467)
- Gronke M., Dijkstra M., McCourt M., Oh S. P., 2017, preprint, preprint (arXiv:1704.06278)
- Haehnelt M. G., 1995, *MNRAS*, 273, 249
- Harrington J. P., 1973, *MNRAS*, 162, 43
- Hartwig T., et al., 2016, *MNRAS*, 462, 2184
- Helgason K., Ricotti M., Kashlinsky A., Bromm V., 2016, *MNRAS*, 455, 282
- Hummer D. G., 1962, *MNRAS*, 125, 21
- Inayoshi K., Haiman Z., Ostriker J. P., 2016, *MNRAS*, 459, 3738
- Johnson J. L., Dijkstra M., 2017, *A&A*, 601, A138
- Johnson J. L., Haardt F., 2016, *Publ. Astron. Soc. Australia*, 33, e007
- Kashlinsky A., Arendt R. G., Mather J., Moseley S. H., 2005, *Nature*, 438, 45
- Li Y., et al., 2007, *ApJ*, 665, 187
- Lodato G., Natarajan P., 2006, *MNRAS*, 371, 1813
- Loeb A., Furlanetto S. R., 2013, *The First Galaxies in the Universe*. Princeton Univ. Press, Princeton, NJ
- Matthee J., Sobral D., Santos S., Röttgering H., Darvish B., Mobasher B., 2015, *MNRAS*, 451, 400
- Mayer L., Kazantzidis S., Escala A., Callegari S., 2010, *Nature*, 466, 1082
- McKee C. F., Tan J. C., 2008, *ApJ*, 681, 771
- Milosavljević M., Bromm V., Couch S. M., Oh S. P., 2009, *ApJ*, 698, 766
- Mortlock D. J., et al., 2011, *Nature*, 474, 616
- Natarajan P., Pacucci F., Ferrara A., Agarwal B., Ricarte A., Zackrisson E., Cappelluti N., 2017, *ApJ*, 838, 117
- Neufeld D. A., 1990, *ApJ*, 350, 216
- Neufeld D. A., 1991, *ApJ*, 370, L85
- Oh S. P., Haiman Z., 2002, *ApJ*, 569, 558
- Omukai K., 2001, *ApJ*, 546, 635
- Osterbrock D. E., 1962, *ApJ*, 135, 195
- Osterbrock D. E., Ferland G. J., 2006, *Astrophysics of gaseous nebulae and active galactic nuclei*, 2nd edn. University Science Books, Sausalito, CA
- Pacucci F., Volonteri M., Ferrara A., 2015a, *MNRAS*, 452, 1922
- Pacucci F., Ferrara A., Volonteri M., Dubus G., 2015b, *MNRAS*, 454, 3771
- Pacucci F., Pallottini A., Ferrara A., Gallerani S., 2017, *MNRAS*, 468, L77
- Pallottini A., et al., 2015, *MNRAS*, 453, 2465
- Raiter A., Schaerer D., Fosbury R. A. E., 2010, *A&A*, 523, A64
- Regan J. A., Haehnelt M. G., 2009, *MNRAS*, 396, 343
- Regan J. A., Visbal E., Wise J. H., Haiman Z., Johansson P. H., Bryan G. L., 2017, *Nature Astronomy*, 1, 0075
- Rivera-Thorsen T. E., et al., 2015, *ApJ*, 805, 14

- Schleicher D. R. G., Spaans M., Glover S. C. O., 2010, *ApJ*, 712, L69
- Seaton M. J., 1955, *Proceedings of the Physical Society A*, 68, 457
- Shibuya T., et al., 2017, preprint, 1705, arXiv:1705.00733
- Smidt J., Wiggins B. K., Johnson J. L., 2016, *ApJ*, 829, L6
- Smidt J., Whalen D. J., Johnson J. L., Li H., 2017, preprint (arXiv:1703.00449)
- Smith A., Safronek-Shrader C., Bromm V., Milosavljević M., 2015, *MNRAS*, 449, 4336
- Smith A., Bromm V., Loeb A., 2016, *MNRAS*, 460, 3143
- Smith A., Bromm V., Loeb A., 2017a, *Astronomy & Geophysics*, 58, 3.22
- Smith A., Bromm V., Loeb A., 2017b, *MNRAS*, 464, 2963
- Sobral D., Matthee J., Darvish B., Schaerer D., Mobasher B., Röttgering H. J. A., Santos S., Hemmati S., 2015, *ApJ*, 808, 139
- Spaans M., Silk J., 2006, *ApJ*, 652, 902
- Springel V., 2010, *MNRAS*, 401, 791
- Stacy A., Greif T. H., Bromm V., 2012, *MNRAS*, 422, 290
- The CGAL Project 2017, CGAL User and Reference Manual, 4.9.1 edn. CGAL Editorial Board, <http://doc.cgal.org/4.9.1/Manual/packages.html>
- Unno W., 1952, *Publications of the Astronomical Society of Japan*, 4, 100
- Visbal E., Haiman Z., Bryan G. L., 2016, *MNRAS*, 460, L59
- Volonteri M., 2012, *Science*, 337, 544
- Wise J. H., Turk M. J., Abel T., 2008, *ApJ*, 682, 745
- Woods T. E., Heger A., Whalen D. J., Haemmerle L., Klessen R. S., 2017, *ApJ*, preprint (arXiv:1703.07480)
- Wu X.-B., et al., 2015, *Nature*, 518, 512
- Wyithe J. S. B., Loeb A., 2012, *MNRAS*, 425, 2892
- Yue B., Ferrara A., Salvaterra R., Xu Y., Chen X., 2013, *MNRAS*, 433, 1556
- Zheng Z., Wallace J., 2014, *ApJ*, 794, 116

This paper has been typeset from a $\text{\TeX}/\text{\LaTeX}$ file prepared by the author.